Chinese Journal of Aeronautics, (2023), 36(9): 178–194

Chinese Society of Aeronautics and Astronautics
& Beihang University

Chinese Journal of Aeronautics

cja@buaa.edu.cn
www.sciencedirect.com

Decomposition of mean skin friction in incident shock wave/turbulent boundary layer interaction flows at Mach 2.25

Junyi DUAN [a,b], **Fulin TONG** [c], **Xinliang LI** [a,b], **Hongwei LIU** [a,*]

[a] *LHD, Institute of Mechanics, Chinese Academy of Sciences, Beijing 100190, China*
[b] *School of Engineering Science, University of Chinese Academy of Sciences, Beijing 100049, China*
[c] *State Key Laboratory of Aerodynamics, China Aerodynamics Research and Development Center, Mianyang 621000, China*

Received 5 September 2022; revised 10 October 2022; accepted 28 November 2022
Available online 22 June 2023

KEYWORDS

Compressible flow;
Boundary layers;
Direct numerical simulation;
Shock waves;
Skin friction;
Turbulent flow

Abstract The evolution characteristics of the mean skin friction beneath the supersonic turbulent boundary layer that interacts with incident shock waves at Mach 2.25 are analyzed using Direct Numerical Simulation (DNS). The separated and attached boundary layers in the interaction region that respectively correspond to 33.2° and 28° incident shock angles are considered. The mean skin friction recovery rate for the separated boundary layer is much gentler and distinctly less than that for the attached case where the skin friction completes its recovery within one boundary layer thickness. The novel mean skin friction decomposition method for compressible flows proposed by the recent research is applied in the interaction region to investigate the internal evolution characteristics quantitatively. The results reveal that the three decomposition components are distinctly unequal between the two cases. The contributions of the turbulent motions at different scales to the associated term are focused on using empirical mode decomposition technology. It indicates that the outer large-scale structures dominate separation and reattachment regions, while contributions from inner small-scale structures are limited. In contrast, contributions from the outer large-scale structures are dramatically reduced in the attached case, which results in the outer large-scale and inner small-scale motions being of equal importance.

1. Introduction

Owing to its ubiquitous presence and profound significance in the aeronautical field, Shockwave/Turbulent Boundary Layer Interactions (STBLIs) have been widely studied over the past half century. The encountered phenomena include the maximum surface fluctuating pressure, severe wall heat flux peak, and strong unsteadiness, which cause significant adverse effects on aircraft and component performance.[1,2] There has been some remarkable progress with these fundamental phenomena, especially over the last 20 years, through the fast-developing high-resolution experimental measurement facilities and High-Performance Computing (HPC) technologies. However, many challenges urgently need to be solved,[3] such

* Corresponding author.
E-mail address: hliu@imech.ac.cn (H. LIU).

https://doi.org/10.1016/j.cja.2023.06.015

as shock wave low-frequency oscillations, turbulence amplification, and quick and accurate prediction methods.

Wall Shear Stress (WSS), together with Wall Heat Flux (WHF) and wall pressure, which are wall-quantities closely related to the aerodynamic design and thermal protection of the aircraft, is of obvious importance in studying wall-bounded turbulent flows.[4,5] A considerable number of empirical or semi-theoretical formulations between mean WSS and Reynolds number in smooth-wall-bounded turbulent flows have been built up.[6–9] Besides, various studies have been conducted to improve understanding of the statistics and structure of fluctuating WSS.[10–12] Extremely high WSS events in the incompressible Turbulent Boundary Layer (TBL) were studied by Pan and Kwon,[10] and the relationships between the extreme positive WSS events and the strong sweeping events originating from the outer layer positive large-scale motions were detected. Statistical characteristics of WSS and WHF fluctuations in supersonic TBL were investigated by Tong et al.,[11] and the similar mechanism for WSS in compressible flows was found through conditional average analysis.

The WSS has also been widely investigated in STBLI flows. Various kinds of methods, for instance, the buried wire gages,[13] laser interferometric instruments,[14] and global interferometry skin friction techniques,[15] were used to make measurements in the two- or three-dimensional interaction regions. The WSS was calculated theoretically for the normal shock wave/flat plate TBL interactions by asymptotic methods.[16] The statistical characteristics of WSS fluctuations, including the probability density function, weighted power-spectrum density, and space–time correlation, are significantly changed through the interaction region.[17,18]

It is well known that the enhanced skin friction and heat transfer in the Reattached Boundary Layer (RBL) can be several times the values of the incoming undisturbed TBL,[19] which deteriorate significantly for hypersonic flows.[20,21] The excessive skin friction causes reduced aerodynamic efficiency and combat radius and increased fuel investments. To the authors' knowledge, there is minimal systematic research about the skin friction evolution characteristics of the TBL under shock interactions. Recent research has proven that skin friction is related to turbulent motion within the boundary layer through mathematical derivations.[22,23] As noted by Tong et al.,[24,25] the turbulent vortex structures are significantly strengthened due to the shock interactions. Turbulent motion within the RBL is more complex and characterized by regenerated small-scale structures in the inner layer, and large-scale structures in the outer layer originating from the upstream interaction region. The relationship between the mean skin friction and complex vortical structures within the RBL needs further study.

The primary objective of this study is to further improve the physical understanding of the skin friction relaxation process downstream of the interaction region in STBLI flows via Direct Numerical Simulation(DNS). To this end, the mean skin friction decomposition in the compressible boundary layer proposed by Li et al.[26] is combined with bidimensional Empirical Mode Decomposition (EMD) to analyze the DNS dataset of the 33.2°/28° incident shock that interacts with a turbulent boundary layer at Mach 2.25. This method can provide a physical interpretation for different contributing terms while quantifying the contributions associated with specific spanwise length scales.

The remainder of this paper is organized as follows. Section 2 fully describes the simple flow configuration selected for the DNS and the adopted computational setup. Section 3 discusses the evolution characteristics of the mean skin friction in STBLI flows through analyses of the ensemble-averaged field, mean skin friction decomposition, and empirical mode decomposition. Conclusions are drawn in Section 4.

2. Numerical strategy

2.1. DNS setup overview

The three-dimensional compressible conservative Navier-Stokes equations are nondimensionalized using the freestream velocity u_∞, density ρ_∞, temperature T_∞, dynamic viscosity μ_∞, and unit length $L = 1\ \text{in}^{-1}$ (1 in = 0.0254 m), and are directly numerically solved using the high-order finite difference solver Opencfd-SC developed by Li et al.,[27] which has been widely applied in compressible turbulent flows and STBLI flows.[28–32] The subscript "∞" represents the properties of the freestream flow. The perfect gas equation and Sutherland's equation are employed to close the governing equations. The specific heat ratio and molecular Prandtl number are taken as $\gamma = 1.4$ and $Pr = 0.7$ respectively. For the spatial discretization of the governing equations, the convection terms are solved using a bandwidth-optimized WENO scheme combined with the limiters,[33] which has been generally used in STBLI problems.[17,34] The diffusion terms are solved using an eighth-order central scheme. In addition, a third-order Runge-Kutta method is used for time integration.

A two-dimensional sketch of the computational domain is shown in Fig. 1. The original point of the Cartesian coordinate system is at the nominal shock incident point x_o, and the spatial coordinates are normalized by the turbulent boundary layer thickness $\delta_{ref} = 0.078\ \text{in}^{-1}$ at the reference station, where its non-dimensional coordinate is $x = -4.0$. Unless otherwise stated, the spatial coordinates (x, y, z) are normalized by δ_{ref}. The laminar boundary layer, which has identical freestream parameters and wall temperature conditions, is prescribed at the inlet boundary. A fully developed TBL is generated through the transition of the incoming laminar boundary layer under the disturbance of wall blowing and suction. The region for these disturbances ranges from $x = -47.5$ to -41.1 downstream of the inflow laminar boundary layer, and the setup of wall-normal disturbance velocity v_{bs} is the same as suggested by Pirozzoli et al.[35] and Fang et al.[36] Additionally, an isothermal non-slip boundary condition with a fixed wall temperature of $T_w = 1.9T_\infty$ is imposed. Hereafter, the subscript "w" denotes the properties at the wall surface. The non-reflective boundary condition is adopted for the computational domain's outlet and top far-field boundaries to protect it from staining by reflected disturbances. The single-point R-H relations are imposed at the top boundary around $x_s = -9.8$ or -12.1 to generate an incident shock with shock angles of $\alpha = 33.2°$ or 28°. The incident shock generated by this method is easier to control than the wedge angle used by Zhong et al.[37] Periodic boundary conditions are used in the spanwise direction.

As shown in Fig. 1, the extent of the computational domain is $L_x \times L_y \times L_z = 68.43\delta_{ref} \times 6.31\delta_{ref} \times 2.25\delta_{ref}$. A structured Cartesian mesh composed of $3700 \times 300 \times 250$ grid points in

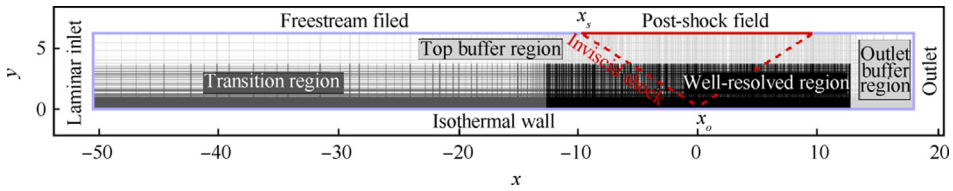

Fig. 1 Sketch of computational domain in x-y plane. The grid points are plotted with only every tenth and fourth point in x and y directions, respectively.

the x, y, and z directions discretizes the computational domain for both cases. The mesh in the streamwise direction is progressively refined in the transition region ranging from $x = -51.3$ to -12.8 (total of 600 grid points) and is uniformly distributed in the well-resolved region ranging from $x = -12.8$ to 12.8 (total of 3000 grid points). In these two regions, the wall-normal mesh is clustered toward the wall using a hyperbolic tangent mapping with 193 grid points within the TBL and 280 grid points within the computational domain ($y \leq 3.85$). In the top and outlet buffer regions, the mesh is rapidly coarsened in the wall-normal (20 grid points) and streamwise (100 grid points) directions respectively to further perfect the dominating computational region from being fouled by reflected disturbances. In addition, 250 grid points are equally distributed for the spanwise computational domain $0 \leq z \leq 2.25$. As evaluated at the reference station, the mesh resolution in the streamwise direction, wall-normal directions at wall surface and TBL edge, and the spanwise direction are $\Delta x^+ = 6.23$, $\Delta y_w^+ = 0.65$, $\Delta y_e^+ = 11.66$, and $\Delta z^+ = 6.54$, respectively. Note that the superscript "+" represents the variable in the inner scaling, i.e., it is normalized with the viscous scales computed at the reference station. Research by Poggie et al.[38] on the effects of mesh resolution on compressible turbulent flows indicates that the present simulation uses the standard mesh to resolve the finest structures in turbulent flows.

The parameters of the fully developed TBL are similar to those considered by Pirozzoli et al.[35,39] and Fang et al.[36] These are a freestream Mach number of $Ma_\infty = 2.25$, freestream unit Reynolds number of $Re = 635000\ \text{in}^{-1}$, and freestream flow temperature of $T_\infty = 169.44$ K. At the reference station, the Reynolds number based on the momentum boundary layer thickness is $Re_\theta = \rho_\infty u_\infty \theta/\mu_\infty = 3533$, and the friction Reynolds number is $Re_\tau = \rho_w u_\tau \delta_{\text{ref}}/\mu_w = 728$.

2.2. DNS validation

The van Driest transformed mean streamwise velocity u_{vd}^+ in the inner scaling is defined as

$$u_{\text{vd}}^+ = \int_0^{u^+} \sqrt{\frac{\bar{\rho}}{\bar{\rho}_w}}\,\mathrm{d}\bar{u}^+ \tag{1}$$

and the Reynolds-averaged streamwise velocity $\bar{u}$ in the outer scaling is plotted in Fig. 2. Unless otherwise stated, the superscript bar "–" and tilde "~" represent the Reynolds average (i.e., time-spanwise average) and Favre average (i.e., density-weighted average $\widetilde{\Phi} = \overline{\rho\Phi}/\bar{\rho}$) respectively, with a prime and double prime for the corresponding fluctuations. As shown in Fig. 2, the velocity profiles overlap well with the DNS data from Schlatter and Örlü[9] (incompressible TBL at $Re_\theta = 2000$) and Fang et al.[36] (similar compressible TBL at $Re_\theta = 3700$), as well as the experimental data of Bookey et al.[40] (compressible TBL at $Re_\theta = 2400$). Specifically, the profile of u_{vd}^+ presents a linear distribution in the viscous sublayer $y^+ < 7$ and obeys the log-law with a standard slope of $1/\kappa = 2.44$ (κ is the Karman constant) with a cutoff of 5.2 in the log layer $30 < y^+ < 100$.

The profiles of the local-density weighted Reynolds stress components $\bar{\rho}/\bar{\rho}_w\widetilde{u''u''}$, $\bar{\rho}/\bar{\rho}_w\widetilde{v''v''}$, $\bar{\rho}/\bar{\rho}_w\widetilde{w''w''}$, and $\bar{\rho}/\bar{\rho}_w\widetilde{u''v''}$ for the fully developed TBL are presented in Fig. 3. A good quantitative agreement between the present DNS and the results of Schlatter and Örlü[9] and Fang et al.[36] is achieved. Furthermore, the peak of the streamwise normal stress $\bar{\rho}/\bar{\rho}_w\widetilde{u''u''}$ is located in the buffer region at $y^+ \approx 13$, which is coincident with previous results. However, the peak value is slightly greater than that of Schlatter and Örlü[9] due to the Reynolds number effects.

More quantitative evidence is provided in Fig. 4, where the budget terms of the Turbulent Kinetic Energy (TKE) $K = \widetilde{u_i''u_i''}/2$ are reported. The TKE transport equation can be written as

$$\frac{\partial \bar{\rho}K}{\partial t} = C + P + T + \Pi + D + M - \varepsilon \tag{2}$$

where TKE is balanced by the terms of convection C, production of the mean velocity gradient P, turbulent transport T, pressure dilatation Π, viscous diffusion D, mass flux contribution associated with density fluctuations M, and viscous dissipation ε. Detailed formulae for these terms are found in the work of Pirozzoli et al.[35] and Tong et al.[41] As shown in Fig. 4(a), the transport process for TKE is dominated primarily by the production P, viscous dissipation ε, turbulent transport T, and viscous diffusion D, while the other terms are negligible. In the region of $y^+ < 30$, the greatest generation of TKE is transported into the near-wall region via turbulent transport and viscous diffusion, and eventually dissipated as heat in the near-wall region. In the log layer for $y^+ > 30$, TKE production is balanced mainly by viscous dissipation. Furthermore, the production-to-dissipation ratio P/ε is illustrated in Fig. 4(b), which shows that the ratio attains a maximum value of approximately 2.0 at $y^+ \approx 10$. These results are consistent with those of Schlatter and Örlü[9] and Sun et al.[42] In particular, the ratio remains constant for $30 < y^+ < 100$ with a value between 1.0 and 1.2, which implies a local equilibrium in the log layer.

In Fig. 5, the distribution of the mean wall pressure p_w^* for $\alpha = 33.2°$ is compared with the experimental data from Dupont et al.[43] at $Ma = 2.3$ with $\alpha = 33.4°$, and the DNS data of Fang et al.[36] under similar flow conditions. The mean wall pressure is defined as $p_w^* = (\bar{p}_w - p_\infty)/(p_1 - p_\infty)$, where $\bar{p}_w$ is Reynolds-averaged pressure at the wall surface, p_∞ is the pres-

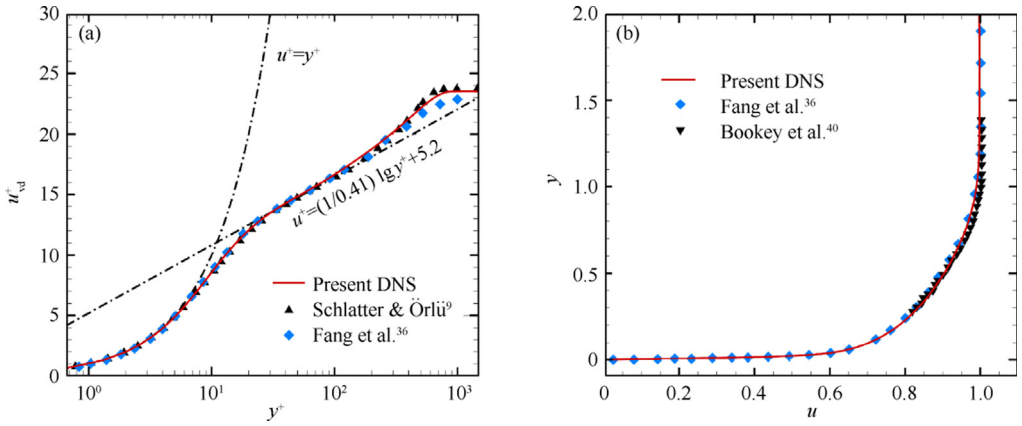

Fig. 2 Profiles of van Driest transformed mean streamwise velocity u^+_{vd} for inner scaling (a) and Reynolds-averaged streamwise velocity $\bar{u}$ for outer scaling (b) at reference station.

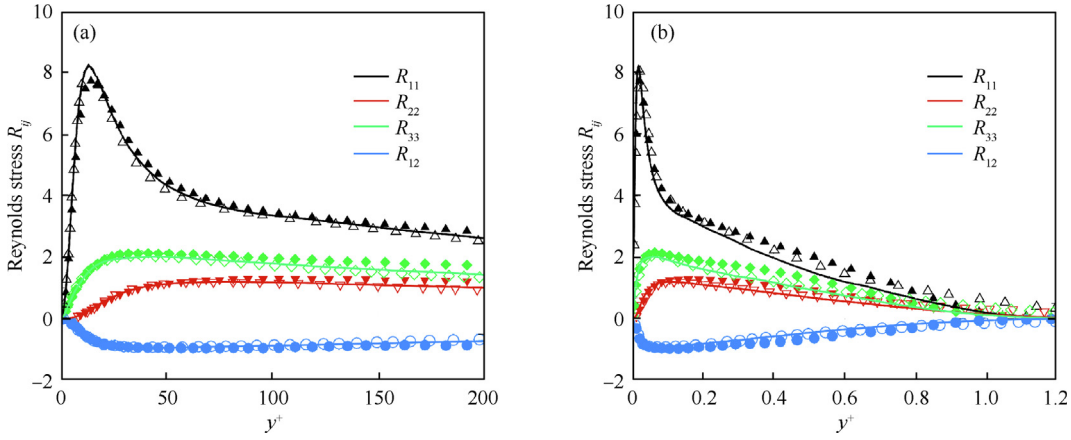

Fig. 3 Profiles of local density-weighted Reynolds stress tensor $R_{ij} = \bar{\rho}/\bar{\rho}_w \widetilde{u_i'' u_j''}$ for inner scaling (a) and outer scalin-g (b) at reference station. The solid and hollow symbols are the DNS results of incompressible TBL conducted by Sch-latter and Örlü[9] and compressible TBL by Fang et al.,[36] respectively.

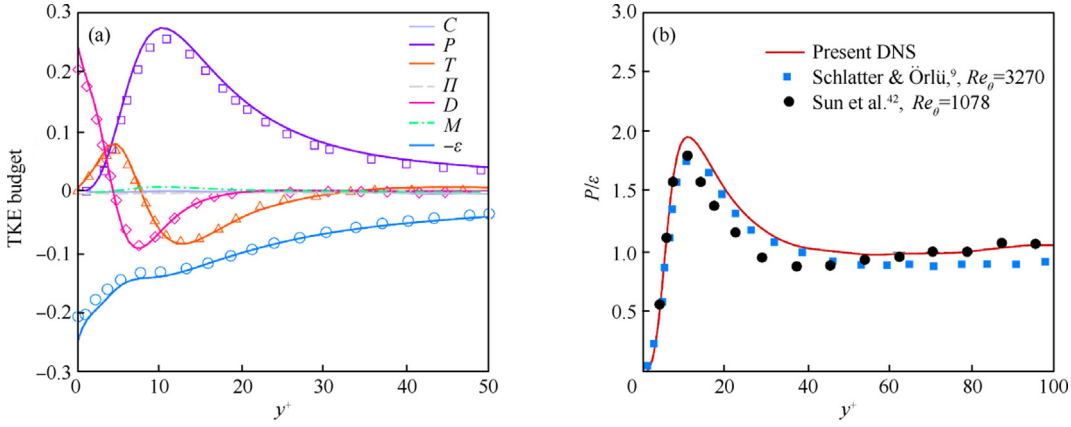

Fig. 4 Profiles of turbulence kinetic energy budget terms (a) and production-to-dissipation ratio (b) at reference station. The symbols in (a) are the DNS results for $Ma = 2.25$ zero-pressure-gradient turbulent boundary layer with the same flow conditions as Pirozzoli et al.[35]

sure of the freestream flow, and p_1 is the pressure after the incident shock, which is calculated using the R-H relations. The origin of the streamwise coordinate in Fig. 5 is set as the mean position of the foot for the reflected shock wave x_{RS}, which is determined as suggested by Fang et al.[36] where the position of the mean wall pressure $\bar{p}_w$ rises to $(p_1 + p_\infty)/2$. A good

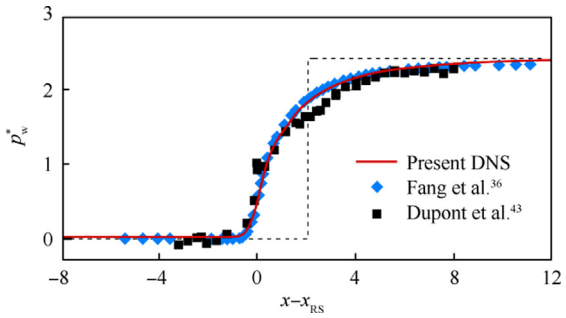

Fig. 5 Distribution of mean wall pressure, $p_w^* = (\bar{p}_w - p_\infty)/(p_1 - p_\infty)$, with the incident shock angle of $\alpha = 33.2°$. The dotted line represents the inviscid shock solution.

collapse between the current DNS with the experimental data and previous DNS data is seen in Fig. 5, which represents the accuracy of the simulation in the interacting region.

3. Results and discussion

3.1. Instantaneous and mean flow fields

Contour maps of the instantaneous streamwise velocity u for $\alpha = 33.2°$ and 28° are plotted in Figs. 6 and 7, respectively. An incident shock is generated through the single-point R-H relations imposed at the top boundary and interacts with the incoming TBL downstream. As shown in Fig. 6(a), a transparent separation region can be observed around the incident shock point. According to Souverein et al.,[44] a strong interaction occurs for $\alpha = 33.2°$. The incoming TBL is blocked under the adverse-pressure-gradient effects caused by the incident shock, and a large area of low-momentum fluids accumulates in the downstream region of the reflected shock. Multiple small and separated elements, which are highlighted by solid white lines, can be found within the separation bubble. Notably, the reattached turbulent structures downstream of the interaction region are lifted by the low-momentum fluids within a long horizontal distance (at least $5\delta_{ref}$).

In the buffer layer, the canonical high- and low-speed alternating streamwise-elongated streak structures with spanwise widths of approximately $\Delta z^+ = 80$–100 are seen in Fig. 6 (b), which is consistent with the experimental observations of compressible TBL at $Ma = 2$ by Ganapathisubramani et al.[45] Despite these streak structures disappear within the interaction region, and they begin to regenerate until $2\delta_{ref}$ downstream of x_o. Furthermore, the regenerated streak structures, such as at $x = 3.0$, have a much larger spanwise scale than the upstream TBL. These are associated with Görtler vortices[20, 46–48] and Kelvin-Helmholtz instability[43, 49] in the detached shear layer, as previously observed by Pasquariello et al.[50]

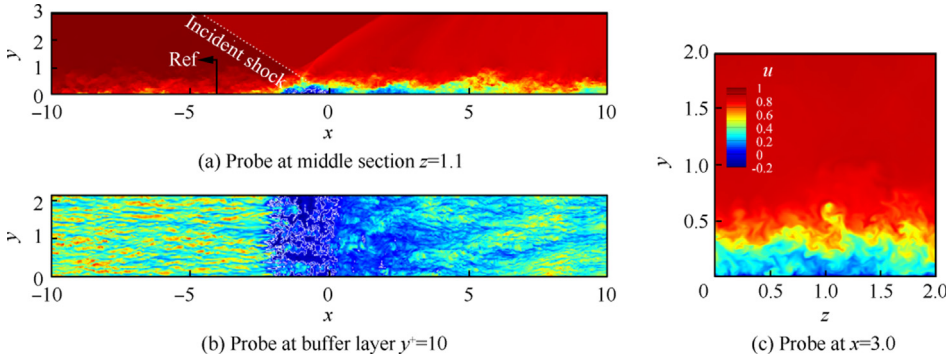

Fig. 6 Contour maps of instantaneous streamwise velocity u for an incident shock angle $\alpha = 33.2°$ in x-y plane (a), x-z plane (b), and y-z plane (c). The white solid lines are the isolines of $u = 0$.

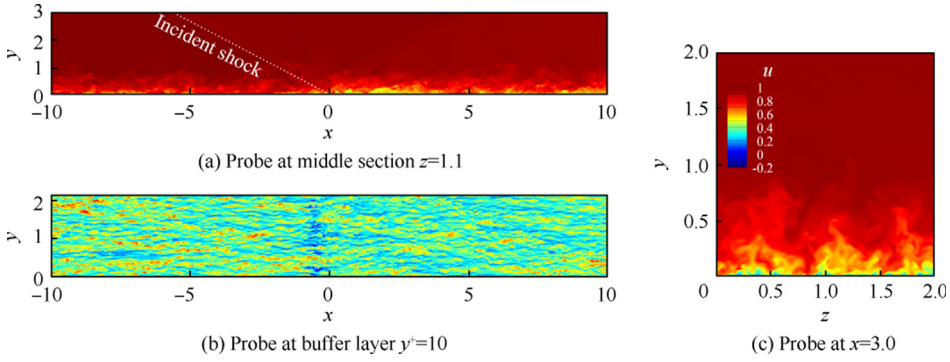

Fig. 7 Contour maps of instantaneous streamwise velocity u for an incident shock angle $\alpha = 28°$ in x-y plane (a), x-z plane (b), and y-z plane (c). The white solid lines are the isolines of $u = 0$.

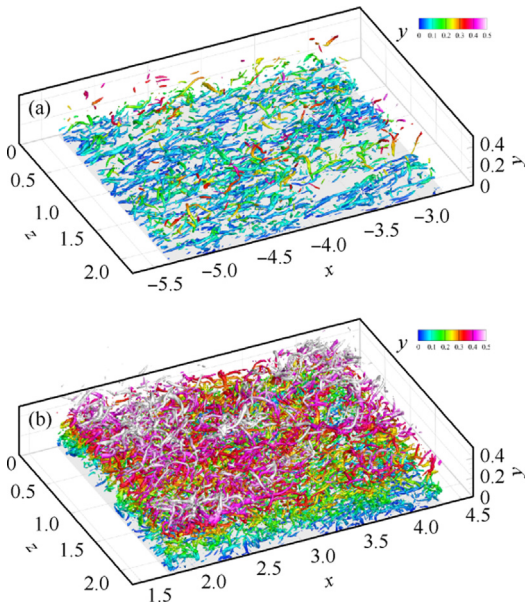

Fig. 8 Instantaneous turbulence coherent structures around reference station (a) and downstream of interaction region (b) for an incident shock angle of $\alpha = 33.2°$.

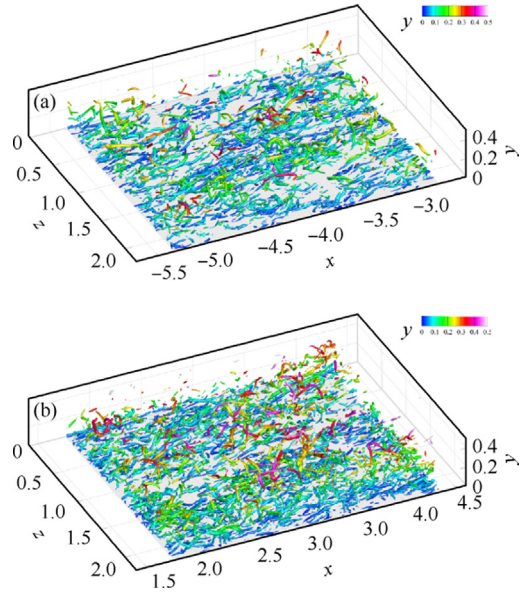

Fig. 9 Instantaneous turbulence coherent structures around reference station (a) and downstream of interaction region (b) for an incident shock angle of $\alpha = 28°$.

As reported in Fig. 7, the interaction intensity for $\alpha = 28°$ is weaker than that for $\alpha = 33.2°$. The large area for low-momentum fluids that is obviously observed in Fig. 6(a) is absent, and the incoming boundary layer remains nearly attached when passing through the interaction region. Moreover, the flow field structure for $\alpha = 33.2°$, which is completely separated in the interaction region, is distinct from the interactions with $\alpha = 28°$, where the fluids have minimal separation. In addition, a footprint of the incident shock brands on the incoming streamwise-elongated structures is shown in Fig. 7 (b), where the lower-speed streaks between $\times = -1.0$ and 0 are relatively weakened. Downstream of the interaction region, these streaky structures are essentially preserved and the spanwise length is slightly changed, which is utterly different from the 33.2° case.

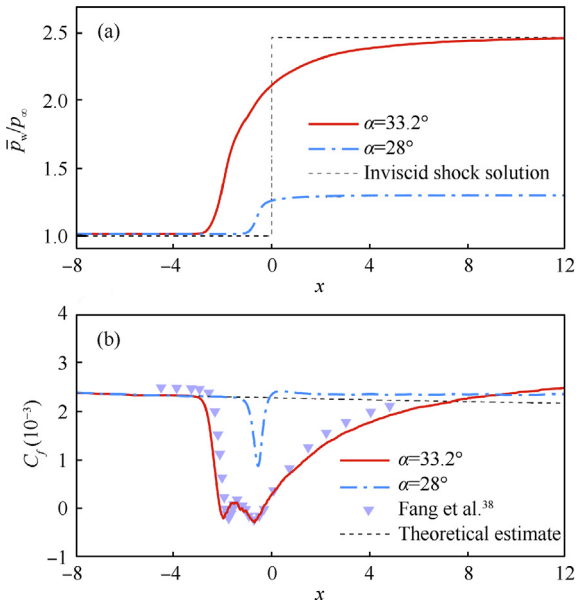

Fig. 10 Distribution of mean wall pressure $\bar{p}_w/p_\infty$ (a) and mean skin friction coefficient C_f (b). The dashed lines in Fig. 10(a) are the inviscid shock solution.

The instantaneous vortex structures beneath the fully developed TBL and RBL for both cases are visualized in Figs. 8 and 9, respectively, using the Q criterion proposed by Jeong and Hussain.[51] Coherent structures appear as streamwise vortices upstream of the interaction region, which is known as the leg of horseshoe-like vortices and agrees with the numerical observations of Zhang et al.,[52] Wu et al.,[53] and Fang et al.,[36] as well as the experimental observations by Zhuang et al.[54] For $\alpha = 33.2°$, there are more vortex structures captured at higher altitudes around $x = 3$, with larger spatial scales than at the upstream TBL, which is consistent with observations of the streak structures in the near-wall region. However, differences in the vortex structures between the upstream and downstream zone are indistinctive for $\alpha = 28°$, except that the vortices downstream of the interaction region are slightly more abundant and at approximately the same height as the upstream ones.

Fig. 10 illustrates the distribution of the mean wall pressure $\bar{p}_w/p_\infty$ and mean skin friction coefficient, defined as $C_f = \tau_w/\left((1/2)\rho_\infty u_\infty^2\right)$, where τ_w is the streamwise components of WSS. Compared with the inviscid shock solution, we find that the distribution of $\bar{p}_w/p_\infty$ in Fig. 10(a) is significantly impacted by the viscous effect, which spreads the wall pressure jump over a much larger area with a smoother gradient. Furthermore, the skin friction reported in Fig. 10(b) drops as the wall pressure increases after entering the interaction region,

which indicates that the boundary layer decelerates under the effects of the adverse pressure gradient. Specifically, for $\alpha = 28°$, the skin friction quickly decreases to 38% of its incoming level before the incident shock point and then recovers quickly to its nominal value after the incident shock point. No negative skin friction is observed in the interaction region, indicating that the boundary layer is statistically fully attached across the interaction. However, for $\alpha = 33.2°$, the skin friction drops sharply but becomes negative before rising to a minimal positive value. After this brief rise, the skin friction reduces to a negative value before increasing to a positive one. The distribution of the mean skin friction predicts two distinct separation bubbles, which is consistent with the observations of Fang et al.[36]

Clearly, the streamwise distributions of the skin friction in the downstream region for both cases are distinct. To intuitively evaluate the streamwise evolution process of the skin friction, a theoretical estimate proposed by White[55] for the undisturbed TBL is plotted in Fig. 10(b) with the dashed line,

$$C_f = \frac{0.455}{S^2}\left[\lg\left(\frac{0.06}{S}(Re_x - Re_{x_0})\frac{\bar{\mu}_e}{\bar{\mu}_w}\sqrt{\frac{\bar{T}_e}{\bar{T}_w}}\right)\right]^{-2} \tag{3}$$

where x_0 is the "virtual" origin of the turbulent part of the boundary layer, and

$$S = \frac{1}{\arcsin A}\sqrt{\frac{\bar{T}_w}{\bar{T}_e} - 1} \text{with} A = \left(\frac{\gamma - 1}{2} Ma_e^2 \frac{\bar{T}_e}{\bar{T}_w}\right)^{1/2} \tag{4}$$

Pirozzoli et al.[35] showed good agreement between the above formula and its DNS results, thus providing a reference skin friction value for the downstream undisturbed TBL. For $\alpha = 28°$, the dropped skin friction recovers sharply to a value of approximately 2.3×10^{-3}, and then decreases gradually farther downstream. In contrast, for $\alpha = 33.2°$, the entire recovery process for the skin friction is gentle. The skin friction experiences a consistent increase downstream of the interaction region and does not rise to the same level as the upstream TBL until $x = 7.4$, which then presents a continuously increasing trend. In summary, the recovery process for the skin friction in the separated boundary layer is relatively distinct from that in the attached boundary layer. In addition, the skin friction of the downstream disturbed TBL for both cases are more significant than that of the undisturbed TBL calculated from Eq. (3), although under the blockage effects caused by the incident shock.

3.2. Mean skin friction decomposition

The mean skin friction coefficient is defined as the ratio between the mean wall shear stress τ_w and freestream dynamic pressure, i.e., $C_f = \tau_w/\left((1/2)\rho_\infty u_\infty^2\right)$, where the mean wall shear stress is calculated as $\tau_w = \bar{\mu}_w \partial \bar{u}/\partial y|_{\text{wall}}$. According to recent research,[22,23,26] the mean skin friction in wall-bounded turbulent flow can be decomposed into different physics-informed contributions based on the mean and statistical turbulence quantities across the wall layer. For compressible turbulent boundary layer flow, the mean skin friction decomposition equation proposed by Li et al.[26] is

$$C_f = \underbrace{\frac{2}{\rho_\infty u_\infty^3}\int_0^\delta \bar{\tau}_{yx}\frac{\partial \widetilde{u}}{\partial y}\mathrm{d}y}_{C_{f,\mathrm{V}}} + \underbrace{\frac{2}{\rho_\infty u_\infty^3}\int_0^\delta \bar{\rho}\,\widetilde{-u''v''}\frac{\partial \widetilde{u}}{\partial y}\mathrm{d}y}_{C_{f,\mathrm{T}}}$$
$$+ \underbrace{\frac{2}{\rho_\infty u_\infty^3}\int_0^\delta (\widetilde{u} - u_\infty)\left[\bar{\rho}\left(\widetilde{u}\frac{\partial \widetilde{u}}{\partial x} + \widetilde{v}\frac{\partial \widetilde{u}}{\partial y}\right) - \frac{\partial}{\partial x}\left(\bar{\tau}_{xx} - \bar{\rho}\,\widetilde{u''u''} - \bar{p}\right)\right]\mathrm{d}y}_{C_{f,\mathrm{G}}} \tag{5}$$

Three contributions in Eq. (5) are: $C_{f,\mathrm{V}}$, which represents the direct viscous dissipation effect; $C_{f,\mathrm{T}}$, which represents the power spent for turbulent kinetic energy production; $C_{f,\mathrm{G}}$, which represents the spatial growth of the flow, including the flow convection, streamwise heterogeneity, and pressure gradient.

The decomposition results for the fully developed TBL at the reference station of $x = -4$ are given in Table 1, compared with those of compressible zero-pressure-gradient flat plate TBL from Fan et al.[56] at $Ma = 2$ and $Re_\tau = 580$, and Tong et al.[11] at $Ma = 2.25$ and $Re_\tau = 769$. All three components positively contribute to skin friction generation, which is closely consistent with the previous studies. The TKE-production $C_{f,\mathrm{T}}$ and direct dissipation $C_{f,\mathrm{V}}$ are the predominant components, which yield up to 46.6% and 40.8% of C_f, respectively. Contribution coming from the spatial growth $C_{f,\mathrm{G}}$ can be neglected, only reaching 12.6% of C_f. Figs. 11 and 12 show the decomposed components of the skin friction at different streamwise locations for both cases, respectively. The relative error in this research is calculated as $100 \times (C_{f,\mathrm{V}} + C_{f,\mathrm{T}} + C_{f,\mathrm{G}} - C_f)/C_f$ %. The errors at all locations for both cases are negligibly small and generally confined to ± 3%, reflecting the accuracy of the decomposition method in STBLI flows.

The mean skin friction decomposition results in the interaction region for $\alpha = 33.2°$ are plotted in Fig. 11. $C_{f,\mathrm{V}}$ and $C_{f,\mathrm{T}}$ are positive contributions, while $C_{f,\mathrm{G}}$ negatively contributes to the skin friction generation in the interaction region, which closely resembles the decomposition results in adverse-pressure-gradient TBL as developed on flat-plates and airfoils.[57] In general, the absolute values of $C_{f,\mathrm{T}}$ and $C_{f,\mathrm{G}}$ increase significantly in the separation region and become far larger than C_f, whereas a rapid decrease is observed in the reattachment region. The trend for $C_{f,\mathrm{V}}$ exhibits an opposite behavior.

Compared with the upstream TBL, a completely different scenario emerges in the separation region characterized by small negative skin frictions, where large positive TKE-production and large negative spatial growth dominate. Specifically, the positive direct dissipation $C_{f,\mathrm{V}}$ experiences a sharp decrease, and its contribution is negligible, whereas the spatial growth $C_{f,\mathrm{G}}$ becomes negative and takes the leading role in the skin friction generation. These counteract the significantly

Table 1 Decomposed skin friction components for fully developed turbulent boundary layer.

Case	$C_{f,\mathrm{V}}/C_f$ (%)	$C_{f,\mathrm{T}}/C_f$ (%)	$C_{f,\mathrm{G}}/C_f$ (%)
Present DNS	40.76	46.61	12.63
Fan et al.[56]	40.53	49.50	9.96
Tong et al.[11]	41.73	45.02	13.25

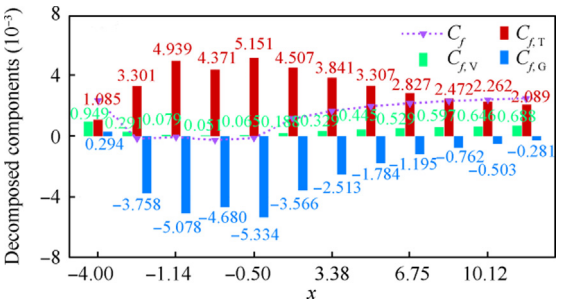

Fig. 11 Decomposed skin friction components in interaction region for $\alpha = 33.2°$.

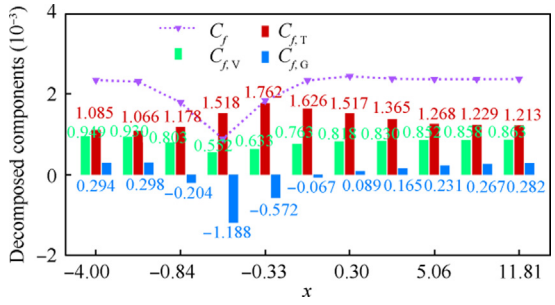

Fig. 12 Decomposed skin friction components in interaction region for $\alpha = 28°$.

amplified positive TKE-production. For instance, at $x = -0.75$, the absolute values of $C_{f,T}$ and $C_{f,G}$ are much greater than C_f by one order of magnitude.

In the reattachment region, the predominance of $C_{f,G}$ is gradually overtaken by the increased positive $C_{f,V}$ and decreased $C_{f,T}$, which causes a consistently increased positive C_f that appears from $x = 1.69$ to 11.81. Two observations are made regarding this behavior. First, despite the magnitudes of both $C_{f,T}$ and $C_{f,G}$ experiencing a consistent decrease, the attenuation of $C_{f,G}$ is greater than that of $C_{f,T}$, whereby the positive $C_{f,T}$ plays a dominant role in the skin friction generation. As seen in Fig. 11, at $x = 1.69$, $C_{f,T}$ and $C_{f,G}$ have comparable magnitudes only in the initial part of the reattachment region. However, at $x = 11.81$ and downstream of the reattachment region, $C_{f,G}$ is dramatically reduced with only 7.9% remaining, while $C_{f,T}$ decreases to 46.4% of its value at $x = 1.69$. Second, the positive contribution of $C_{f,V}$ becomes apparent. At $x = 11.81$, the magnitude of $C_{f,V}$ is approximately 2.5 times larger than that for $C_{f,G}$, which contributes to 27.6% of C_f.

Fig. 12 shows similar trends for $\alpha = 28°$ at the direct viscous dissipation $C_{f,V}$, TKE-production $C_{f,T}$, and spatial growth $C_{f,G}$. Specifically, before $x = -0.33$ and around the nominal shock incident point, $C_{f,T}$ increases sharply and then consistently decreases in the downstream region, whereas $C_{f,V}$ and $C_{f,G}$ hold opposite behavior. However, the contributions of the three terms for the C_f generation change completely. As mentioned above, $C_{f,V}$ is negligible in the separation region and gradually takes a predominant role in the farther downstream reattachment region. For $\alpha = 28°$, $C_{f,V}$ is comparable with $C_{f,T}$ at $x = 0.3$. It is the initial part of the recovering boundary layer and contributes to 33.4% of C_f, much greater than that in Fig. 11.

Moreover, $C_{f,T}$ and $C_{f,G}$ become relatively less predominant. For instance, the maximum value of $C_{f,T}$ in Fig. 12 appears at $x = -0.33$, which is only 1.6 times that of the upstream TBL and much less than 4.8 times that for $\alpha = 33.2°$. Although $C_{f,G}$ is also gradually increased downstream of the interaction region, it has a small positive contribution to C_f generation for $\alpha = 28°$. In general, the dramatically increased $C_{f,V}$ and relatively high $C_{f,T}$ lead to the rapid recovery of C_f, despite $C_{f,G}$ having a negative contribution.

3.3. EMD analysis of TKE-production contributions

Empirical mode decomposition is an adaptive mode decomposition method first proposed by Huang et al.[58] EMD directly extracts intrinsic mode functions based on the signal's instantaneous features, unlike Fourier analyses that require a set of basis functions in advance. Thus, EMD is a data-driven and posteriori method for data analysis. Readers can refer to the work of Huang et al.[58] and Cheng et al.[59] for more details about EMD procedures. It is inherently suitable for non-stationary and non-linear processes like those in turbulent flows. The advantages in processing multiscale signals have led to EMD being applied extensively in fluid mechanics.[10,11,59,60] Recently, attached eddies with specific length scales in turbulent channel flows were identified by Cheng et al.[59] using bidimensional EMD. The contributions of these structures to skin friction generation were quantitatively evaluated.

Here, the scale decomposition of the turbulent motion is achieved by employing bidimensional EMD technology to investigate the contribution of the turbulent fluctuations at different length scales in the interaction region to C_f generation in STBLI flows. The velocity fluctuations u" and v" in the y-z plane are decomposed into four EMD modes, which is different from that of Cheng et al.[59] who decomposed velocity fluctuations in the homogeneous directions (x-z) of channel flows. Furthermore, different from Tong et al.,[24] to have a more comprehensive understanding of the skin friction generation characteristics in the STBLI flows, the situation in the reattachment region is analyzed, and the separation region is included. In addition, an extra case without flow separation is conducted to evaluate the effect of the interaction strength on the results.

Contour maps of the spanwise premultiplied energy spectra of the original full and decomposed velocity fluctuations as functions of the spanwise wavelength λ_z^+ and y^+ at the reference station are shown in Figs. 13 and 14, respectively. The energy spectra are calculated from $(\bar{\rho}/\bar{\rho}_w)k_z\Phi$, where k_z is the spanwise wavenumber and Φ is the Fourier spectra of the velocity fluctuations.

The full spanwise premultiplied energy spectra, together with the decomposed spectra, are plotted in Fig. 13. The spectra of u" shown in Fig. 13(a) exhibit a primary energy peak with a spanwise wavelength of $\lambda_z^+ \approx 100$ at $y+ \approx 12$, which corresponds to the near-wall high- and low-speed streaks. The relatively high Reynolds number of $Re_\tau = 730$ gives a secondary peak with a spanwise wavelength of $\lambda_z^+ \approx 550$ at $y^+ \approx 120$. It is ascribed to the generation of large-scale energy-

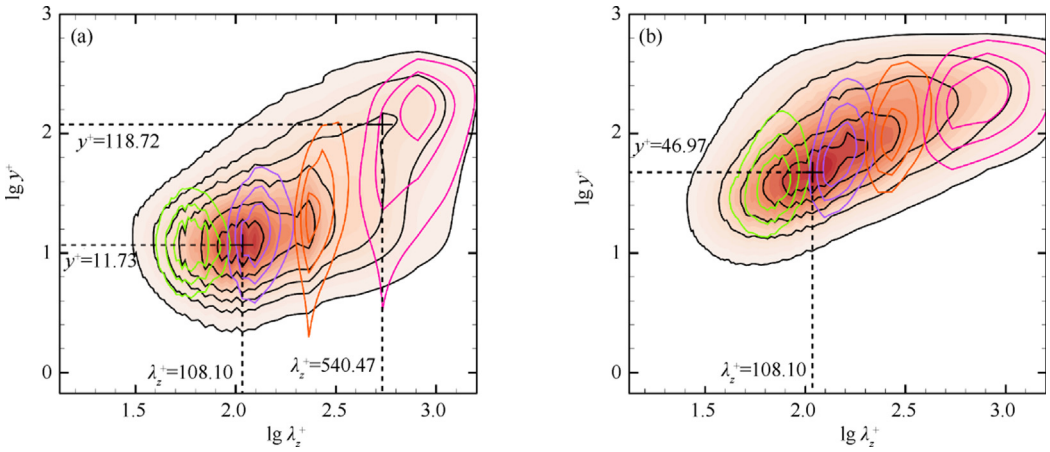

Fig. 13 Spanwise premultiplied energy spectra of streamwise velocity fluctuations (a) and wall-normal velocity fluctuati-ons (b) at reference station. The black lines represent the original DNS case. The green, purple, orange and pink lines represent Modes 1 to 4, respectively.

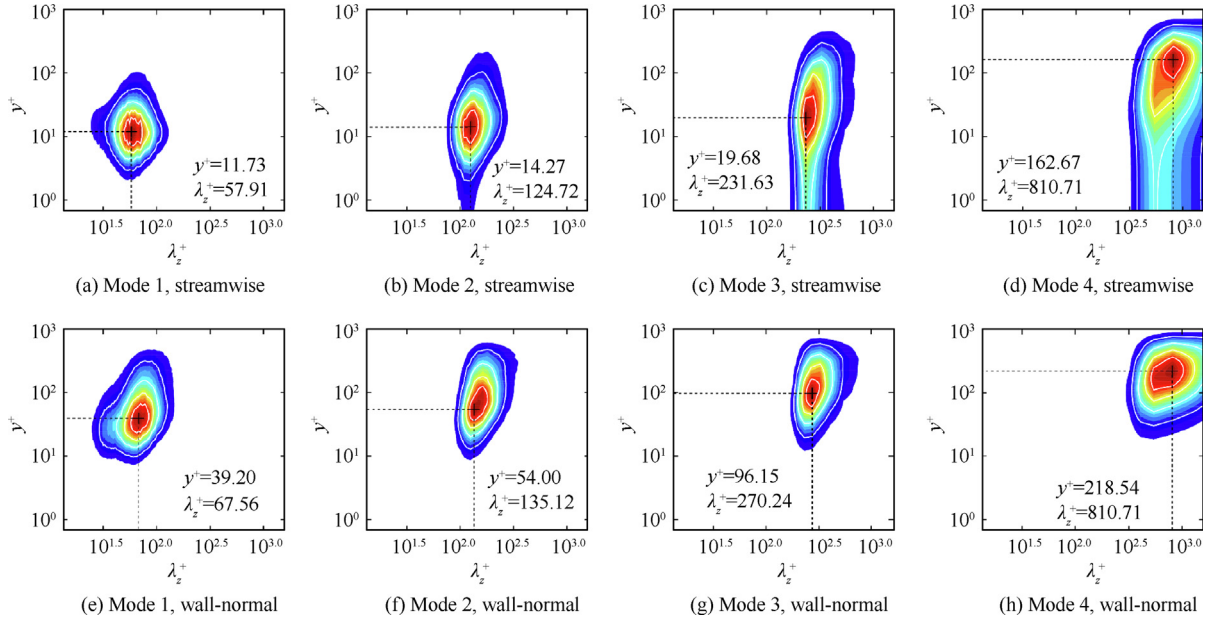

Fig. 14 Spanwise premultiplied energy spectra at reference station: (a)-(d) spectra of decomposed streamw-ise velocity fluctuations u_d'' in Modes 1 to 4, respectively; (e)-(h) spectra of decomposed wall-normal ve-locity fluctuations v_d'' in Modes 1 to 4, respectively.

carried turbulent motion in high Reynolds number flows. For the spectra of v", only one primary energy peak with a wavelength of $\lambda_z^+ \approx 47$ at $y^+ \approx 108$ is seen in Fig. 13(b). Our results agree well with those of Tong et al.[24] Additionally, the decomposed results effectively capture the general trend of the entire spectra. The turbulent fluctuations are separated into four modes, characterized by different specific spanwise length scales, which suggests that EMD decomposition is suitable for scale decomposition.

The spectrum contour maps presented in Figs. 14(a) and (b) reveal that the spectra of u_d'' are located within the near-wall region with a peak at $y^+ \approx 12$ for Mode 1 and $y^+ \approx 15$ for Mode 2 with spanwise length scales of $\lambda_z^+ \approx 60$ and $\lambda_z^+ \approx 130$, respectively. Hereafter, the subscript "d" denotes the EMD decomposed part of velocity fluctuations, whereas the spectra of v_d'' in Modes 1 and 2 are more intense across the buffer layer, and the peak is at $y^+ \approx 40$–50 with a similar spanwise length scale as u_d''. Cheng et al.[59] supported the first and second EMD modes for u_d'' to represent the near-wall streaky structures, while v_d'' and w_d'' represent quasi-streamwise vortices. Despite the spanwise velocity fluctuations w_d'' not being analyzed in this study, the spectra for the velocity fluctuations in Mode 3 are located at a higher location with a peak at $y^+ \approx 20$ for u_d'' and $y^+ \approx 100$ for v_d''. Similarly, u_d'' and v_d'' have approximately the same peak spanwise wavelength. According to Cheng et al.,[59] the third mode is representative of self-similar attached eddies at the log layer. The spectral results in mode 4 show that u_d'' and v_d'' are located at the higher region, and peaks at the wake layer have a common largest length scale of $\lambda_z^+ \approx 810$. Cheng et al.[59] have shown that the last mode

characterizes the Large Structure Motions (LSM) and Very Large Structure Motions (VLSM) in the wall-bounded turbulent flows. Overall, the decomposed results in our study are consistent with the results of Cheng et al.[59]

To further assess the contributions of turbulent fluctuations to different length scales on the mean skin friction generation, the corresponding Reynolds Shear Stress (RSS) is calculated using u_d'' and v_d''. As analyzed above, velocity fluctuations are separated into four EMD modes. Full velocity fluctuations have the relations:

$$\begin{cases} u'' = u_1'' + u_2'' + u_3'' + u_4'' \\ v'' = v_1'' + v_2'' + v_3'' + v_4'' \end{cases} \tag{6}$$

where the number subscript represents velocity fluctuations in the corresponding EMD mode. Hence, the Reynolds shear stress $-\widetilde{u''v''}$ can be decomposed into 16 components as four primary parts and 12 cross parts representing interactions among different scales. These 16 parts of the RSS, the reconstructed RSS, and the original RSS are plotted in Fig. 15. The profiles of the original and reconstructed RSS collapse well with each other, which indicates the correctness of our EMD analysis. In addition, we find that the four primary parts dominate at different heights, whereas the 12 cross parts are almost negligible.

Then, the $C_{f,\mathrm{T}}$ term related to the TKE-production can be recalculated based on the decomposed RSS components, which is associated with different-scale motions as

$$C_{f,\mathrm{T}i} = \frac{2}{\rho_\infty u_\infty^3} \int_0^\delta \bar{\rho} \, -\widetilde{u_m'' v_n''} \frac{\partial \widetilde{u}}{\partial y} \mathrm{d}y \tag{7}$$

where the subscripts $i = 1, 2, \ldots, 16$ have the following relationship with the mode number m and n: $i = 4m + n - 4$. The 16 parts of the contribution computed by $100 \times C_{f,\mathrm{T}i}/C_{f,\mathrm{T}}$ % are shown in Fig. 16. The primary parts $C_{f,\mathrm{T}1}$, $C_{f,\mathrm{T}6}$, and $C_{f,\mathrm{T}16}$ provide the top three contributions to the $C_{f,\mathrm{T}}$ term, whereas the primary part $C_{f,\mathrm{T}11}$ is less significant. Moreover, the cross parts represent interactions between two adjacent modes, i.e., $C_{f,\mathrm{T}2}$, $C_{f,\mathrm{T}5}$, $C_{f,\mathrm{T}7}$, $C_{f,\mathrm{T}10}$, $C_{f,\mathrm{T}12}$, and $C_{f,\mathrm{T}15}$, which can provide limited contributions. However, the cross parts represent interactions between two nonadjacent modes, i.e., $C_{f,\mathrm{T}3}$, $C_{f,\mathrm{T}4}$, $C_{f,\mathrm{T}8}$, $C_{f,\mathrm{T}9}$, $C_{f,\mathrm{T}13}$, and $C_{f,\mathrm{T}14}$, which can be neglected.

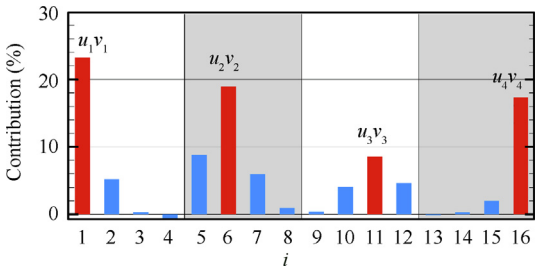

Fig. 16 Contributions of Reynolds shear stress shown in Fig. 15 to $C_{f,\mathrm{T}}$.

In general, the majority of $C_{f,\mathrm{T}}$ have contributions from the parts associated with the inner structures, including the primary parts $C_{f,\mathrm{T}1}$ and $C_{f,\mathrm{T}6}$, as well as the cross parts $C_{f,\mathrm{T}2}$ and $C_{f,\mathrm{T}5}$, which even includes $C_{f,\mathrm{T}7}$ and $C_{f,\mathrm{T}10}$. These give a total contribution of 66.2%. Thus, we believe $C_{f,\mathrm{T}}$ is dominated by near-wall small-scale turbulent motion upstream of the fully developed TBL. Additionally, secondary contributions are from $C_{f,\mathrm{T}11}$, $C_{f,\mathrm{T}12}$, $C_{f,\mathrm{T}15}$, and $C_{f,\mathrm{T}16}$ at 32.6%. It indicates that large-scale motion at the outer layer and interactions between them with motion within the boundary layer are significant in high Reynolds number flows. Similarly, Li et al.[26] also found a secondary peak at the premultiplied integrands function of $C_{f,\mathrm{T}}$ when the Reynolds number is up to $Re_\tau = 800$ when considering the impact of the Reynolds number on the mean skin friction in compressible channel flows.

The full and decomposed spectra at the separation region of $x = -0.75$ for $\alpha = 33.2°$ are respectively reported in Figs. 17 and 18. The length scales are normalized by the viscous length scales calculated at the reference station in the following energy spectrum analysis. Two noteworthy phenomena are observed. First, as shown in Fig. 17(a), the near-wall primary peak of the energy spectra for u'', which is observed at the upstream TBL, is absent at the separation region. It indicates that the near-wall streak structures are destroyed in the separation region, consistent with the instantaneous streamwise velocity distribution reported in Fig. 6(b). Second, most energy is concentrated at higher locations with a peak at $y^+ \approx 220$ ($y \approx 0.3$, in the outer scaling) for a larger spanwise length scale. The outer peak of the energy spectra reflects the

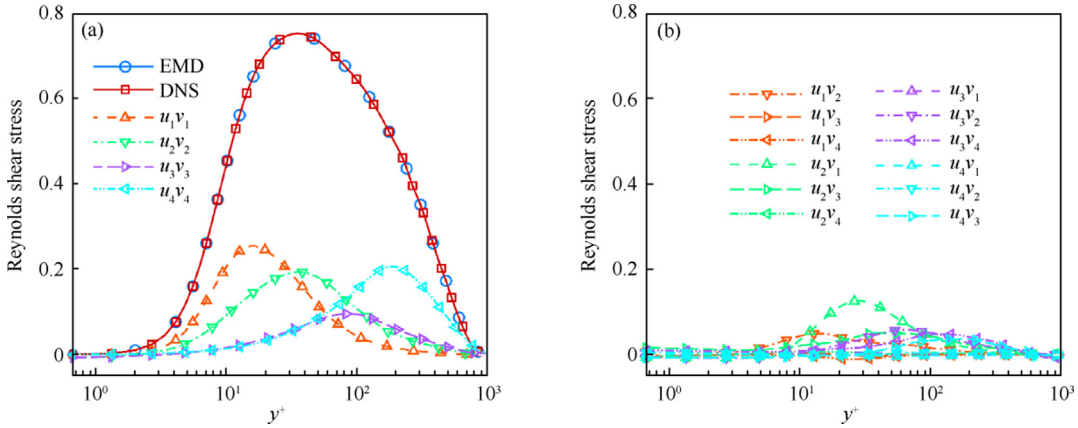

Fig. 15 Profile of Reynolds shear stress calculated from decomposed velocity fluctuations $-\widetilde{u_d''v_d''}/u_\tau^2$ at reference station, (a) for primary terms and (b) for cross terms.

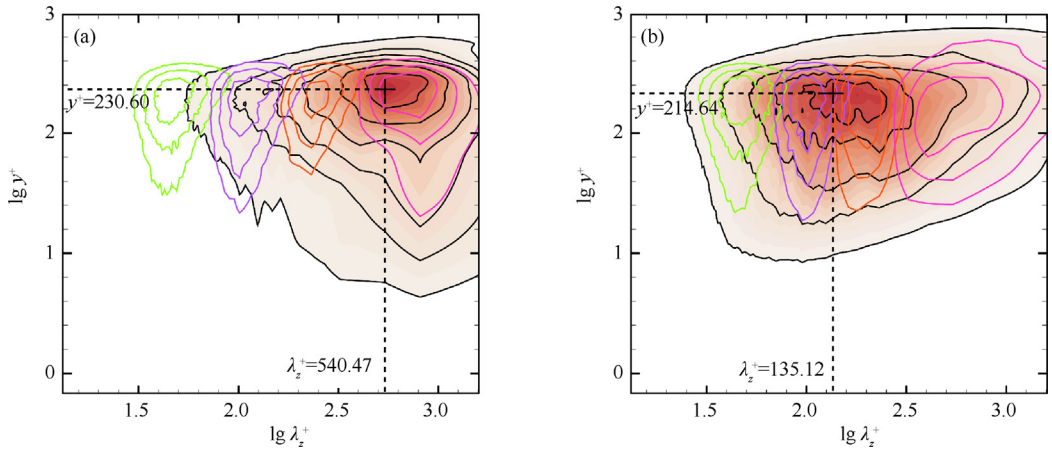

Fig. 17 Spanwise premultiplied energy spectra of streamwise velocity fluctuations (a) and wall-normal velocity fluctuations (b) at $x = -0.75$ for $\alpha = 33.2°$. The black lines represent the original DNS case, and the green, purple, orange, and pink lines represent Modes 1 to 4, respectively.

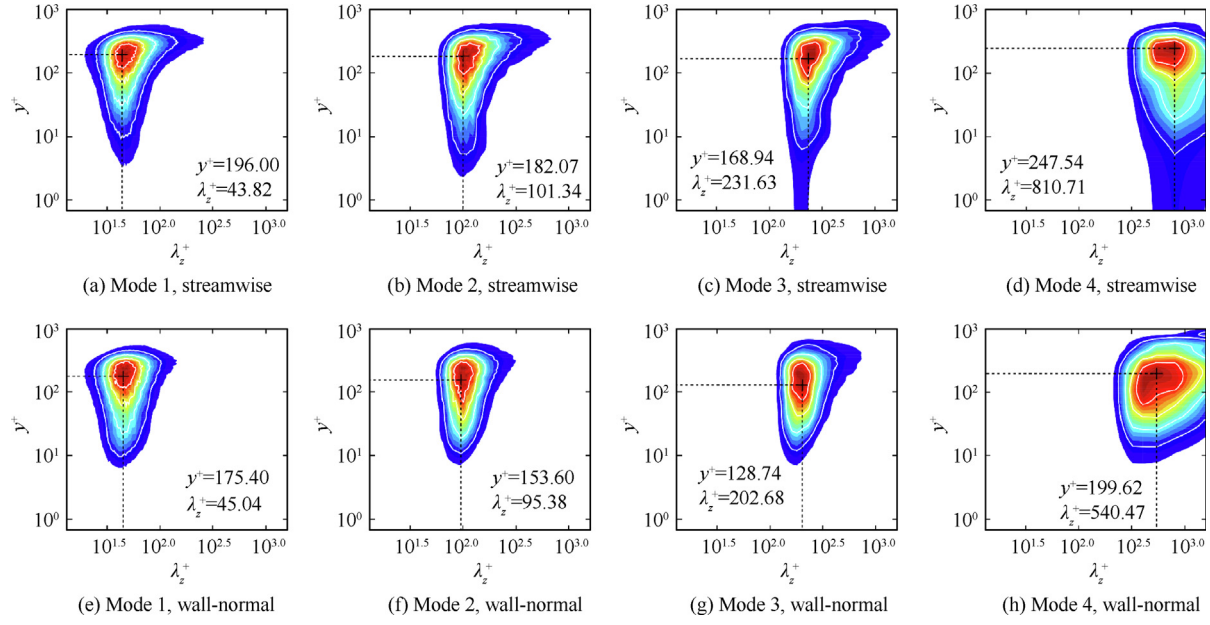

Fig. 18 Spanwise premultiplied energy spectra at $x = -0.75$ for $\alpha = 33.2°$: (a)-(d) spectra of decomposed streamwise velocity fluctuations u_d'' in Modes 1 to 4, respectively; (e)-(h) spectra of decomposed wall-no-rmal velocity fluctuations v_d'' in Modes 1 to 4, respectively.

characteristics of the intense velocity fluctuations within the detached shear layer.

The energy spectra of u_d'' and v_d'' plotted in Fig. 18 show that the peak locations for four modes are ruleless, which is different from the upstream TBL. The appearance of recirculation flows greatly increases the complexity of turbulence in the wall-normal direction, but it can be seen that the peak location is approximately at the same height. Moreover, we find that the characteristic wavelengths for each mode differ from each other and gradually increase.

As shown in Fig. 19, the RSS amplitude at the separation region for $\alpha = 33.2°$ is amplified approximately two times that of the upstream TBL. The turbulence amplification phenomenon in the interaction region is one of the primary characteristics of STBLI flow, which is generally observed via numerical simulations and experimental research.[36,53,61,62] Research on the characteristics of RBL by Tong et al.[24,25] indicates that turbulent motion is associated with the TKE-production term $C_{f,\mathrm{T}}$ and plays an important role in C_f generation in STBLI flows. Section 3.2 shows that the magnified turbulence contributes greatly to the generation of C_f through the mean skin friction decomposition analysis, regardless of whether flow separation occurs. In Fig. 19, the original RSS is dominated by the four primary parts, while the 12 cross parts are relatively insignificant. The peak of the four primary parts is approximately at the same height, consistent with the

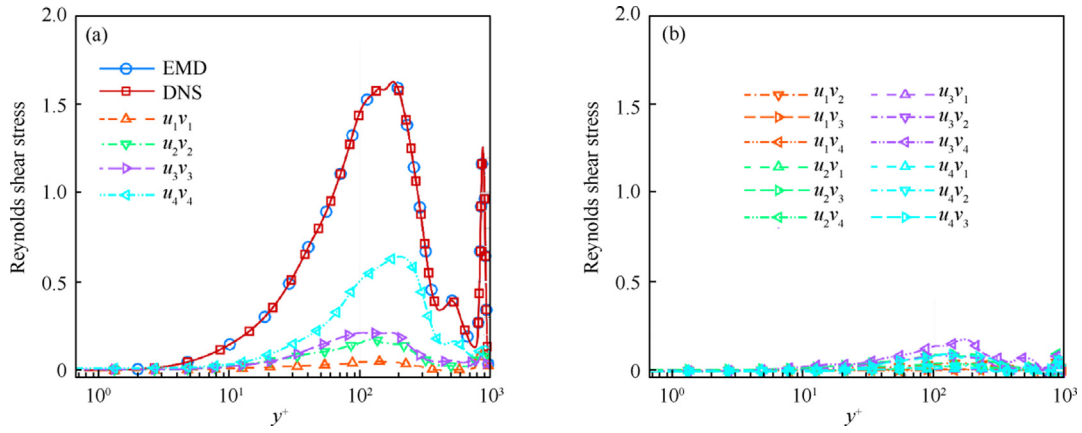

Fig. 19 Profile of Reynolds shear stress as calculated from decomposed velocity fluctuations $-\widetilde{u_d''v_d''}/u_\tau^2$ at $x = -0.75$ for $\alpha = 33.2°$, (a) for primary terms and (b) for cross terms.

observation of energy spectra. Notably, the fourth primary part occupies most of the original RSS at a greater height far from the wall surface.

The 16 parts that contribute to the $C_{f,\mathrm{T}}$ term as calculated from the decomposed RSS are plotted in Fig. 20. The parts associated with small-scale structures are dominated at the upstream TBL, involving the primary parts $C_{f,\mathrm{T1}}$ and $C_{f,\mathrm{T6}}$, as well as the cross parts $C_{f,\mathrm{T2}}$ and $C_{f,\mathrm{T5}}$, but are not prominent in the separation region with a total contribution of only about 19.7%. In contrast, the parts associated with large-scale structures dominate. Even the single part $C_{f,\mathrm{T16}}$ makes up 38%, and the total contributions of the parts associated with large-scale motion, including the primary parts $C_{f,\mathrm{T11}}$ and $C_{f,\mathrm{T16}}$ and cross parts $C_{f,\mathrm{T12}}$ and $C_{f,\mathrm{T15}}$, reach 65.4%. Therefore, we believe that the intense fluctuations within the detached shear layer, generally considered with large spanwise length scales,[63] dominate the $C_{f,\mathrm{T}}$ term contributions in the separation region. The contributions of small-scale motions within the separation bubble are relatively limited.

We show the spanwise premultiplied energy spectra of the original and EMD decomposed velocity fluctuations at the reattachment region of $x = 8.43$ for $\alpha = 33.2°$ in Figs. 21 and 22, respectively. The spectra for u" and v" are shown as black lines in Fig. 21 with both primary peaks located at a higher position of $y^+ \approx 275$. The secondary peaks appear in the near-wall region, which resembles the primary peaks at the upstream TBL and suggests they are regenerated wall-bounded vortical structures. However, the difference between the downstream RBL and upstream TBL is that the energy is concentrated primarily at the outer layer with a relatively large spanwise length scale instead of at the near-wall region with a small scale.

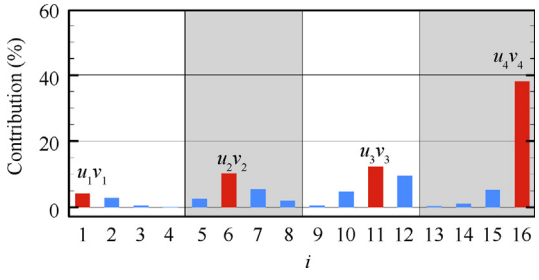

Fig. 20 Contributions of Reynolds shear stress shown in Fig. 19 to $C_{f,\mathrm{T}}$.

The spectra of the velocity fluctuations in the EMD modes are given in Fig. 22. For the streamwise velocity fluctuations, the characteristics (including the peak height and most energy-carried wavelength) of the first two modes at the reattachment region are similar to those at the TBL. We consider that the first two modes still represent the near-wall streak structures shown in Fig. 6(b), but these structures are regenerated and closer to the wall with smaller length scales. Modes 3 and 4 are more complex. As analyzed previously, Mode 3 at the upstream TBL represents the self-similar attached vortices at the log layer, and we believe that this may be available at the reattachment region. However, the higher energy-carried spectra span crosses a large region in the wall-normal direction and extends up to $y^+ \approx 260$. A similar situation is found in mode 4. Thus, we believe that the streamwise velocity fluctuations captured by Modes 3 and 4 are not only regenerated attached vortices but also include large-scale motion as convected from the upstream interaction region. Such energy-spanned phenomena are stronger for the wall-normal fluctuations shown in Figs. 22(e)-(h). Additionally, the most energy-carried wavelengths for different modes are separated as shown in Fig. 21.

The decomposition of the RSS and their contributions to $C_{f,\mathrm{T}}$ term at $x = 8.43$ are shown in Figs. 23 and 24, respectively. The RSS reaches a peak value at a relatively high location of $y^+ = 300$ ($y = 0.4$ in the outer scaling) at the reattachment region. It agrees well with the primary peak of the energy spectra in the outer layer shown in Fig. 21, which further supports the appearance of large-scale vortices in the outer layer. Moreover, the fourth primary part occupies most of the original distribution, which results in the single part $C_{f,\mathrm{T16}}$ contributing to 53.1% of $C_{f,\mathrm{T}}$. However, the total contributions of the primary parts $C_{f,\mathrm{T1}}$ and $C_{f,\mathrm{T6}}$, and cross parts $C_{f,\mathrm{T2}}$ and $C_{f,\mathrm{T5}}$, which represent the near-wall small-scale structures, only occupy 18.7%. In summary, consistent with studies of the RBL conducted by Tong et al.,[24] motion with large-scale length scales in the outer plays the primary role in contributing to the $C_{f,\mathrm{T}}$ term at the reattachment region, while the contribu-

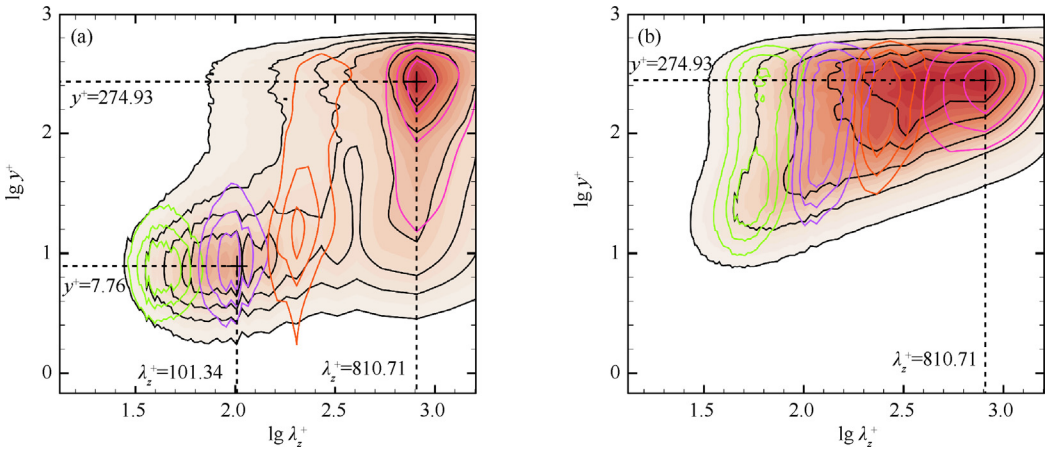

Fig. 21 Spanwise premultiplied energy spectra of streamwise velocity fluctuations (a), and wall-normal velocity fluctuations (b) at $x = 8.43$ for $\alpha = 33.2°$. The black lines represent the original DNS case, and the green, purple, orange, and pink lines represent Modes 1 to 4, respectively.

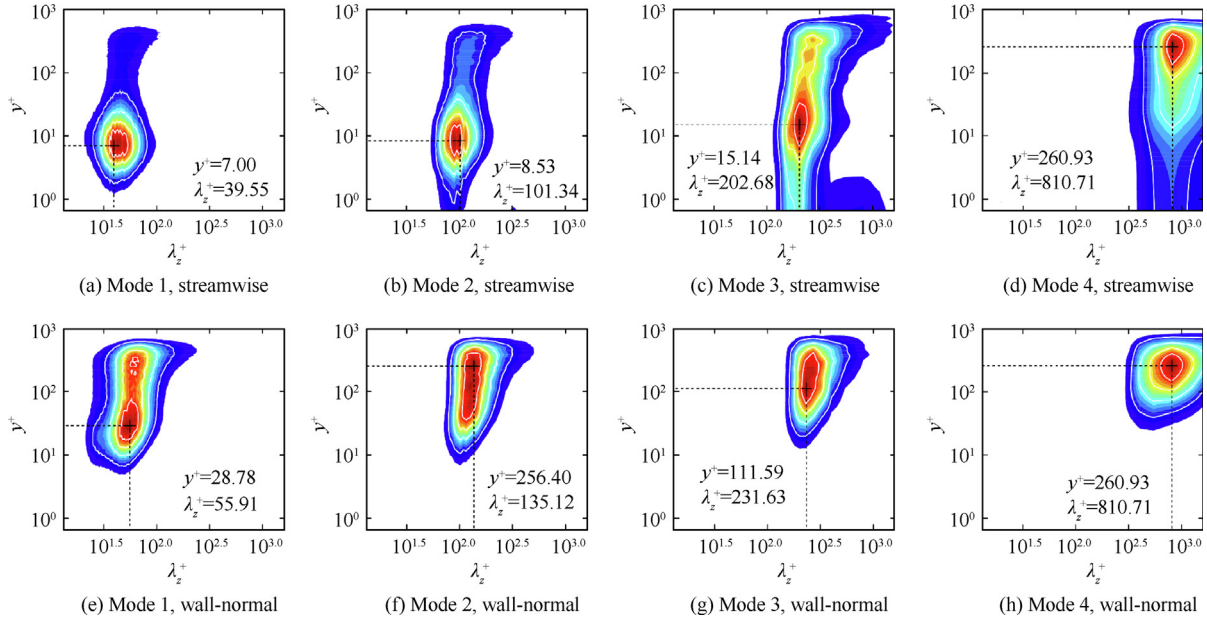

Fig. 22 Spanwise premultiplied energy spectra at $x = 8.43$ for $\alpha = 33.2°$: (a)-(d) spectra of decomposed streamwise velocity fluctuations u_d'' in Modes 1 to 4, respectively; (e)-(h) spectra of decomposed wall-normal velocity fluctuations v_d'' in Modes 1 to 4, respectively.

tions of the near-wall small-scale structures are limited. It contrasts with the upstream TBL, where contributions of the motion with small scales in the near-wall region dominate.

Finally, we consider $\alpha = 28°$ at the same station as analyzed in the reattachment region to compare the effects of flow separation on the skin friction generation. The spanwise premultiplied energy spectra for the full and decomposed velocity fluctuations beneath the boundary layer downstream of the incident shock are shown in Figs. 25 and 26, respectively. Note that there are 19 contour levels of the spectra shown in Figs. 14, 18, 22, and 26 ranging from 10% to 100% of their maximum values. The RSS profile, including the original and decomposed components, and its contribution to the $C_{f,\mathrm{T}}$ term are plotted in Figs. 27 and 28, respectively.

As shown in Figs. 25–28, the characteristics at this station are similar to those at the upstream TBL. However, there are two points worth noting. First, the outlines of the plotted spectra are similar to those at the upstream TBL, as shown in Fig. 25. For streamwise velocity fluctuations, the near-wall primary peak is nearly unaffected, while the secondary peak is stronger and located at a much higher position with a larger length scale. It results in the corresponding changes in the fourth mode. It is plausible that the outer large-scale structures tend to be influenced by the incident shock compared with the inner small-scale turbulence. Second, the maximum value of the RSS is slightly less than that at the upstream TBL, but its trend remains flat across a large region between $y^+ \approx 30$–160. $C_{f,\mathrm{T16}}$ gives the greatest contribution to the $C_{f,\mathrm{T}}$ term at

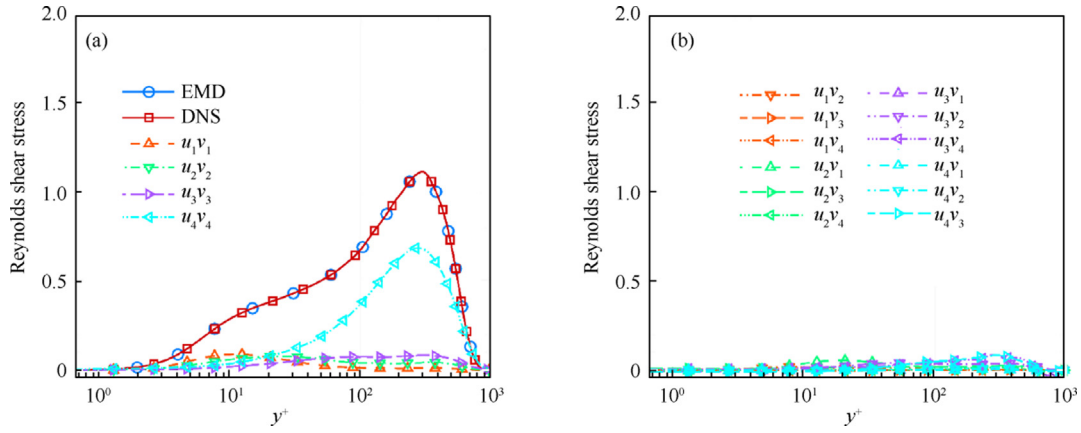

Fig. 23 Profile of Reynolds shear stress as calculated from decomposed velocity fluctuations $-\widetilde{u_d''v_d''}/u_\tau^2$ at $x = 8.43$ for $\alpha = 33.2°$, (a) for primary terms and (b) for cross terms.

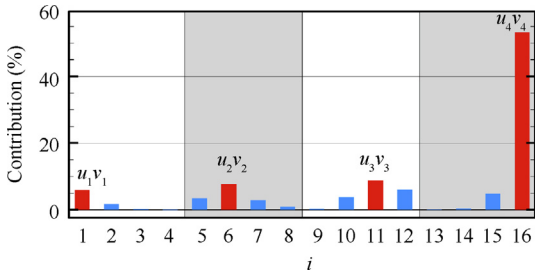

Fig. 24 Contributions of Reynolds shear stress shown in Fig. 23 to $C_{f,\mathrm{T}}$.

up to 26.4% at the downstream boundary layer, which is different from the upstream TBL where $C_{f,\mathrm{T1}}$ provides the greatest contribution at up to 23.2%.

Contributions from near-wall small-scale structures, as represented by the sum of parts $C_{f,\mathrm{T1}}$, $C_{f,\mathrm{T2}}$, $C_{f,\mathrm{T5}}$, and $C_{f,\mathrm{T6}}$, reduce from 56.1% at the upstream TBL to 44% at the downstream boundary layer. Contributions from the large-scale structures in the outer layer, denoted by the sum of parts $C_{f,\mathrm{T11}}$, $C_{f,\mathrm{T12}}$, $C_{f,\mathrm{T15}}$, and $C_{f,\mathrm{T16}}$, increase from 32.5% at the upstream TBL to 44.2%. $C_{f,\mathrm{T}}$ is no longer contributed dominantly by near-wall structures but jointly by the inner and outer structures, which is different from the situation in the reattachment region as analyzed in the previous section. However, we recall that the $C_{f,\mathrm{T}}$ term increases by 13.3% at $x = 8.43$, as analyzed in Section 3. The absolute contribution of the inner small-scale structures to C_f remains nearly constant, but the absolute contribution from the outer large-scale structures is greatly increased. In general, the contributions of the inner and outer structures are comparable to $\alpha = 28°$, which differs from $\alpha = 33.2°$ at which the outer motions dominate C_f generation.

The decomposed results at the same station downstream of the interaction region differ for both cases. In the separated case, large-scale structures are generated within the interaction region through various instabilities, including Kelvin-Helmholtz and centrifugal instabilities, which contribute greatly to the $C_{f,\mathrm{T}}$ term generation. Such large-scale structures can rarely be observed in the attached case, as shown in Fig. 9 (b), and the contributions of the related term are dramatically

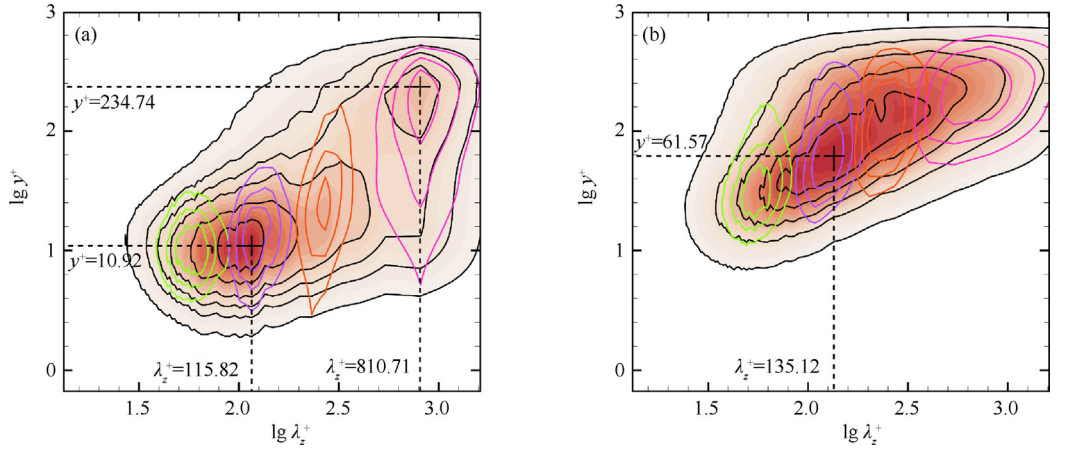

Fig. 25 Spanwise premultiplied energy spectra of streamwise velocity fluctuations (a), wall-normal velocity fluctuations (b) at $x = 8.43$ for $\alpha = 28°$. The black lines represent the original DNS case, and the green, purple, orange, and pink lines represent Modes 1 to 4, respectively.

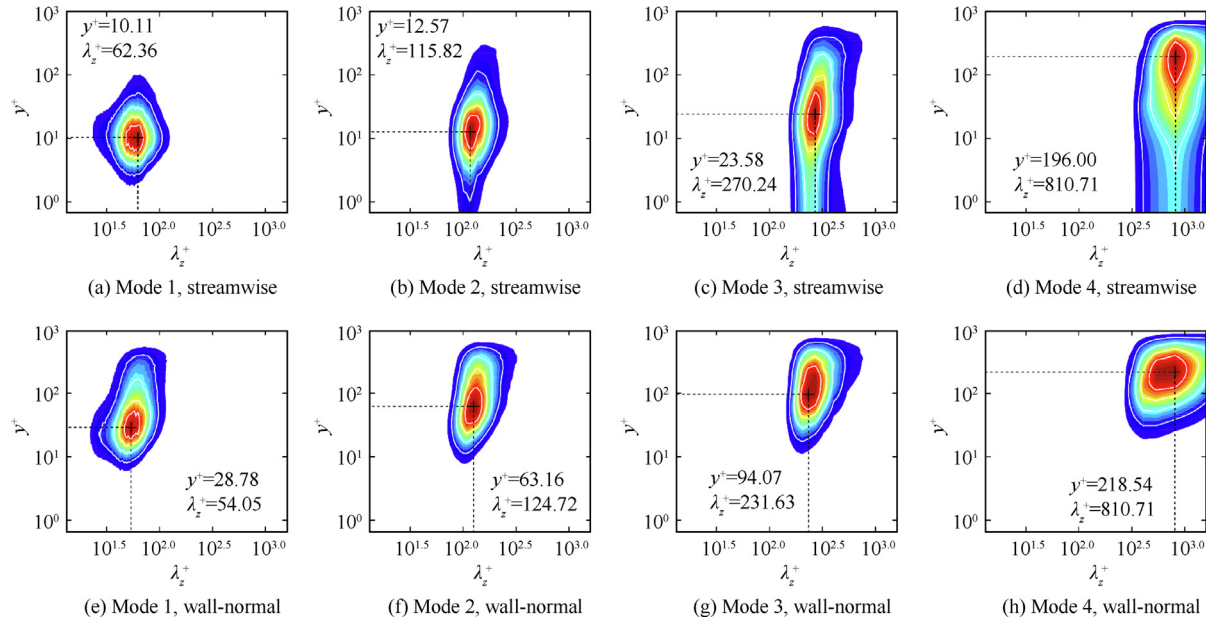

Fig. 26 Spanwise premultiplied energy spectra at $x = 8.43$ for $\alpha = 28°$: (a)-(d) spectra of decomposed streamwise velocity fluctuations u_d'' in Modes 1 to 4, respectively; (e)-(h) spectra of decomposed wall-normal velocity fluctuations v_d'' in Modes 1 to 4, respectively.

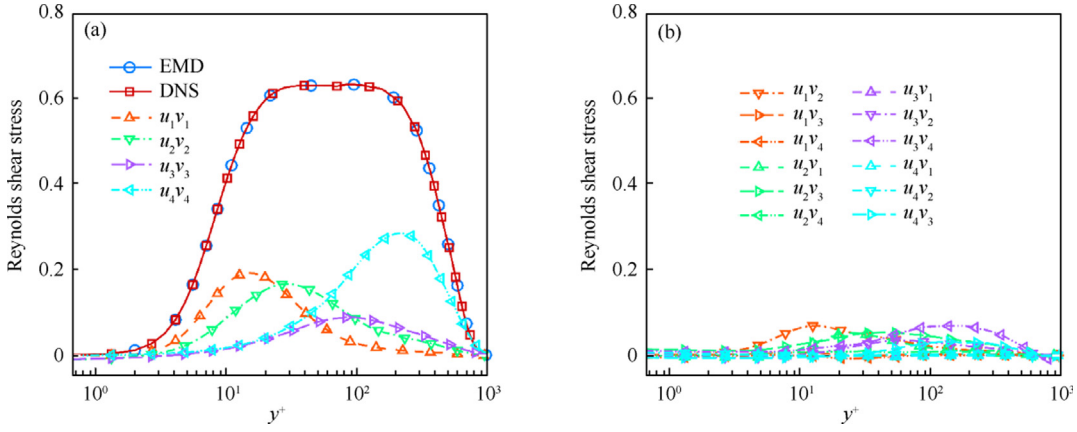

Fig. 27 Profile of Reynolds shear stress calculated from decomposed velocity fluctuations $-\widetilde{u_d''v_d''}/u_\tau^2$ at $x = 8.43$ for $\alpha = 28°$, (a) for primary terms and (b) for cross terms.

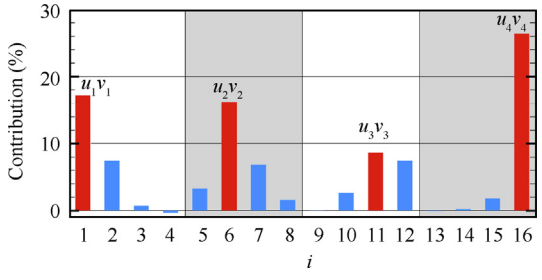

Fig. 28 Contributions of Reynolds shear stress shown in Fig. 27 to $C_{f,\mathrm{T}}$.

reduced. In addition, both the $C_{f,\mathrm{T}}$ term and contributions of the outer large-scale motions to the $C_{f,\mathrm{T}}$ term at the downstream boundary layer are greater than those at the upstream TBL, which is attributed to the effects of turbulence amplification. Thus, the decomposition results between the two cases at the same downstream station are distinct.

4. Conclusions

The mean skin friction evolution characteristics of supersonic shock wave/turbulent boundary layer interactions are investigated using data from the DNS of incident shock waves with

two different incident angles of 33.2° and 28° that interact with a spatially developing boundary layer at $Ma_\infty = 2.25$ and $Re_\tau = 728$. The concluding remarks are given below.

(1) The ensemble-averaged results reveal that the distributions of C_f throughout the interaction region between the two shock angle cases are distinct. For $\alpha = 33.2°$, C_f gradually recovers at the reattachment region and requires at least $7.4\delta_{\text{ref}}$ to retain the same level as the upstream TBL. For $\alpha = 28°$, the TBL remains attached when crossing the incident shock, and C_f quickly recovers within $1\delta_{\text{ref}}$.

(2) The mean skin friction C_f in STBLI flows is decomposed into a viscous dissipation term $C_{f,\text{V}}$, TKE-production term $C_{f,\text{T}}$, and flow spatial growth term $C_{f,\text{G}}$ using the decomposition method proposed by recent research. The decomposition results indicate that the contributions of $C_{f,\text{V}}$ are limited in the case of flow separation, but it still plays an important role when the boundary layer remains attached. The contributions of $C_{f,\text{T}}$ are strengthened in both cases. The maximal magnification factor for $\alpha = 33.2°$ is 4.75 in the separation region and is about 2–3 in the reattachment region. The maximal magnification factor for $\alpha = 28°$ is approximately 1.6 near the shock incident point and 1.1–1.4 downstream of the interaction region. To counter the dramatically enhanced $C_{f,\text{T}}$ term, the absolute value of $C_{f,\text{G}}$ is increased in the case of flow separation, which can negatively contribute to C_f generation.

(3) Bidimensional EMD technology is employed to separate turbulent motion within the interaction region into four modes, characterized by specific spanwise length scales, to investigate further the contributions of different scale motions to the $C_{f,\text{T}}$ term in STBLI flows. For the fully developed TBL, the contributions of inner small-scale motion are dominant, while those of large-scale motion are much weaker. The energy-carried structures with a large spanwise length are observed in the detached shear layer and at the outer layer of the RBL, and their contributions occupy the vast majority of the $C_{f,\text{T}}$ term generation. Those from the inner small-scale structures can be neglected. However, such large-scale structures are absent in the attached case, dramatically reducing their contributions. Even so, the outer and inner motions are equally important, possibly because of the turbulence amplification phenomena.

Declaration of Competing Interest

The authors declare that they have no known competing financial interests or personal relationships that could have appeared to influence the work reported in this paper.

References

1. Dolling DS. Fifty years of shock-wave/boundary-layer interaction research: What next? *AIAA J* 2001;**39**(8):1517–31.
2. Clemens NT, Narayanaswamy V. Low-frequency unsteadiness of shock wave/turbulent boundary layer interactions. *Annu Rev Fluid Mech* 2014;**46**:469–92.
3. Gaitonde DV. Progress in shock wave/boundary layer interactions. *Prog Aerosp Sci* 2015;**72**:80–99.
4. Smits AJ, McKeon BJ, Marusic I. High-Reynolds number wall turbulence. *Annu Rev Fluid Mech* 2011;**43**:353–75.
5. Hwang J, Sung HJ. Wall-attached clusters for the logarithmic velocity law in turbulent pipe flow. *Phys Fluids* 2019;**31**(5):055109.
6. Fernholz HH, Finleyt PJ. The incompressible zero-pressure-gradient turbulent boundary layer: an assessment of the data. *Prog Aerosp Sci* 1996;**32**(4):245–311.
7. Monkewitz PA, Chauhan KA, Nagib HM. Self-consistent high-Reynolds-number asymptotics for zero-pressure-gradient turbulent boundary layers. *Phys Fluids* 2007;**19**(11):115101.
8. Chauhan KA, Monkewitz PA, Nagib HM. Criteria for assessing experiments in zero pressure gradient boundary layers. *Fluid Dyn Res* 2009;**41**(2):021404.
9. Schlatter P, Örlü R. Assessment of direct numerical simulation data of turbulent boundary layers. *J Fluid Mech* 2010;**659**:116–26.
10. Pan C, Kwon Y. Extremely high wall-shear stress events in a turbulent boundary layer. *Journal of Physics: Conference series*; 2017 May 29–Jun 30; Madrid, Spain. Bristol: IOP; 2018.
11. Tong FL, Dong SW, Lai JA, et al. Wall shear stress and wall heat flux in a supersonic turbulent boundary layer. *Phys Fluids* 2022;**34**(1):015127.
12. Guerrero B, Lambert MF, Chin RC. Extreme wall shear stress events in turbulent pipe flows: Spatial characteristics of coherent motions. *J Fluid Mech* 2020;**904**:A18.
13. Murthy VS, Rose WC. Wall shear stress measurements in a shock-wave boundary-layer interaction. *AIAA J* 1978;**16**(7):667–72.
14. Wideman JK, Brown JL, Miles JB, et al. Skin-friction measurements in three-dimensional, supersonic shock-wave/boundary-layer interaction. *AIAA J* 1995;**33**(5):805–11.
15. Schülein E. Skin friction and heat flux measurements in shock/boundary layer interaction flows. *AIAA J* 2006;**44**(8):1732–41.
16. Messiter AF. Interaction between a normal shock wave and a turbulent boundary layer at high transonic speeds. Part I: Pressure distribution. *Zeitschrift Für Angew Math Und Physik ZAMP* 1980;**31**(2):204–26.
17. Tong FL, Duan JY, Li XL. Characteristics of wall-shear stress fluctuations in shock wave and turbulent boundary layer interaction. *J Turbul* 2021;**22**(12):761–83.
18. Tian Y, Han Y, Yang SH, et al. Investigation of fluctuating characteristics of wall shear stress in supersonic flow. *Phys Fluids* 2019;**31**(12):125110.
19. Bernardini M, Asproulias I, Larsson J, et al. Heat transfer and wall temperature effects in shock wave turbulent boundary layer interactions. *Phys Rev Fluids* 2016;**1**(8):084403.
20. Cao SB, Klioutchnikov I, Olivier H. Görtler vortices in hypersonic flow on compression ramps. *AIAA J* 2019;**57**(9):3874–84.
21. Gang DD, Yi SH, Zhang F, et al. Effects of sweep angles on turbulent separation behaviors induced by blunt fin. *Chin J Aeronaut* 2022;**35**(3):90–7.
22. Fukagata K, Iwamoto K, Kasagi N. Contribution of Reynolds stress distribution to the skin friction in wall-bounded flows. *Phys Fluids* 2002;**14**(11):L73–6.
23. Renard N, Deck S. A theoretical decomposition of mean skin friction generation into physical phenomena across the boundary layer. *J Fluid Mech* 2016;**790**:339–67.
24. Tong FL, Duan JY, Li XL. Characteristics of reattached boundary layer in shock wave and turbulent boundary layer interaction. *Chin J Aeronaut* 2022;**35**(6):172–85.
25. Tong FL, Duan JY, Lai J, et al. Hypersonic shock wave and turbulent boundary layer interaction in a sharp cone/flare model. *Chin J Aeronaut* 2023;**36**(3):80–95.
26. Li WP, Fan YT, Modesti D, et al. Decomposition of the mean skin-friction drag in compressible turbulent channel flows. *J Fluid Mech* 2019;**875**:101–23.

27. Li XL, Fu DX, Ma YW, et al. Direct numerical simulation of compressible turbulent flows. *Acta Mechanica Sinica* 2010;**26**(6):795–806.
28. Li X, Tong FL, Yu CP, et al. Statistical analysis of temperature distribution on vortex surfaces in hypersonic turbulent boundary layer. *Phys Fluids* 2019;**31**(10):106101.
29. Li XL, Fu DX, Ma YW. Direct numerical simulation of hypersonic boundary layer transition over a blunt cone with a small angle of attack. *Phys Fluids* 2010;**22**(2):025105.
30. Li XL, Fu DX, Ma YW, et al. Direct numerical simulation of shock/turbulent boundary layer interaction in a supersonic compression ramp. *Sci China Phys Mech Astron* 2010;**53**(9):1651–8.
31. Tong FL, Yu CP, Tang ZG, et al. Numerical studies of shock wave interactions with a supersonic turbulent boundary layer in compression corner: Turning angle effects. *Comput Fluids* 2017;**149**:56–69.
32. Zhu XK, Yu CP, Tong FL, et al. Numerical study on wall temperature effects on shock wave/turbulent boundary-layer interaction. *AIAA J* 2016;**55**(1):131–40.
33. Martín MP, Taylor EM, Wu M, et al. A bandwidth-optimized WENO scheme for the effective direct numerical simulation of compressible turbulence. *J Comput Phys* 2006;**220**(1):270–89.
34. Duan JY, Li X, Li XL, et al. Direct numerical simulation of a supersonic turbulent boundary layer over a compression–decompression corner. *Phys Fluids* 2021;**33**(6):065111.
35. Pirozzoli S, Grasso F, Gatski TB. Direct numerical simulation and analysis of a spatially evolving supersonic turbulent boundary layer at M = 2.25. *Phys Fluids* 2004;**16**(3):530–45.
36. Fang JA, Zheltovodov AA, Yao YF, et al. On the turbulence amplification in shock-wave/turbulent boundary layer interaction. *J Fluid Mech* 2020;**897**:A32.
37. Zhong DD, Wang LX, Ge N. Reflected shock/turbulent boundary layer interaction structure analysis based on large eddy simulation. *Chin J Aeronaut* 2021;**34**(5):364–72.
38. Poggie J, Bisek NJ, Gosse R. Resolution effects in compressible, turbulent boundary layer simulations. *Comput Fluids* 2015;**120**:57–69.
39. Pirozzoli S, Grasso F. Direct numerical simulation of impinging shock wave/turbulent boundary layer interaction at M = 2.25. *Phys Fluids* 2006;**18**(6):065113.
40. Bookey P, Wyckham C, Smits A, et al. New experimental data of STBLI at DNS/LES accessible Reynolds numbers. *43rd AIAA aerospace sciences meeting and exhibit*; 2005 Jan 10-13; Reno, Nevada. Reston: AIAA; 2005.
41. Tong FL, Sun D, Li XL. Direct numerical simulation of impinging shock wave and turbulent boundary layer interaction over a wavy-wall. *Chin J Aeronaut* 2021;**34**(5):350–63.
42. Sun MB, Sandham ND, Hu ZW. Turbulence structures and statistics of a supersonic turbulent boundary layer subjected to concave surface curvature. *J Fluid Mech* 2019;**865**:60–99.
43. Dupont P, Haddad C, Debiève JF. Space and time organization in a shock-induced separated boundary layer. *J Fluid Mech* 2006;**559**:255.
44. Souverein LJ, Dupont P, Debiève JF, et al. Effect of interaction strength on unsteadiness in shock-wave-induced separations. *AIAA J* 2010;**48**(7):1480–93.
45. Ganapathisubramani B, Clemens NT, Dolling DS. Large-scale motions in a supersonic turbulent boundary layer. *J Fluid Mech* 2006;**556**:271.
46. Dussauge JP, Dupont P, Debiève JF. Unsteadiness in shock wave boundary layer interactions with separation. *Aerosp Sci Technol* 2006;**10**(2):85–91.
47. Loginov MS, Adams NA, Zheltovodov AA. Large-eddy simulation of shock-wave/turbulent-boundary-layer interaction. *J Fluid Mech* 2006;**565**:135.
48. Zhuang Y, Tan HJ, Li X, et al. Letter: Görtler-like vortices in an impinging shock wave/turbulent boundary layer interaction flow. *Phys Fluids* 2018;**30**(6):061702.
49. Liu J, Fiscaletti D, Yuan HC. Evolution of turbulent boundary layer over a three-dimensional bump. *Chin J Aeronaut* 2022;**35**(6):137–45.
50. Pasquariello V, Hickel S, Adams NA. Unsteady effects of strong shock-wave/boundary-layer interaction at high Reynolds number. *J Fluid Mech* 2017;**823**:617–57.
51. Jeong J, Hussain F. On the identification of a vortex. *J Fluid Mech* 1995;**285**:69–94.
52. Zhang ZG, Tong FL, Duan JY, et al. Direct numerical simulation of supersonic turbulent expansion corner with shock impingement. *Phys Fluids* 2021;**33**(10):105104.
53. Wu M, Martin MP. Direct numerical simulation of supersonic turbulent boundary layer over a compression ramp. *AIAA J* 2007;**45**(4):879–89.
54. Zhuang Y, Tan HJ, Li X, et al. Letter: Evolution of coherent vortical structures in a shock wave/turbulent boundary-layer interaction flow. *Phys Fluids* 2018;**30**(11):111702.
55. White FM. *Viscous fluid flow*. New York: McGraw–Hill; 1974.
56. Fan YT, Li WP, Pirozzoli S. Decomposition of the mean friction drag in zero-pressure-gradient turbulent boundary layers. *Phys Fluids* 2019;**31**(8):086105.
57. Fan YT, Li WP, Atzori M, et al. Decomposition of the mean friction drag in adverse-pressure-gradient turbulent boundary layers. *Phys Rev Fluids* 2020;**5**(11):114608.
58. Huang NE, Shen Z, Long SR, et al. The empirical mode decomposition and the Hilbert spectrum for nonlinear and non-stationary time series analysis. *Proc R Soc Lond A* 1971;**1998**(454):903–95.
59. Cheng C, Li WP, Lozano-Durán A, et al. Identity of attached eddies in turbulent channel flows with bidimensional empirical mode decomposition. *J Fluid Mech* 2019;**870**:1037–71.
60. Agostini L, Leschziner MA. On the influence of outer large-scale structures on near-wall turbulence in channel flow. *Phys Fluids* 2014;**26**(9):099901.
61. Dolling DS, Or CT. Unsteadiness of the shock wave structure in attached and separated compression ramp flows. *Exp Fluids* 1985;**3**(1):24–32.
62. Dolling DS, Murphy MT. Unsteadiness of the separation shock wave structure in a supersonic compression ramp flowfield. *AIAA J* 1983;**21**(12):1628–34.
63. Mustafa MA, Parziale NJ, Smith MS, et al. Amplification and structure of streamwise-velocity fluctuations in compression-corner shock-wave/turbulent boundary-layer interactions. *J Fluid Mech* 2019;**863**:1091–122.